Atomic Structural Models of Fibrin Oligomers

Artem Zhmurov[1,2], **Anna D. Protopopova**[3], **Rustem I. Litvinov**[3,4], **Pavel Zhukov**[1], **John W. Weisel**[3,*], and **Valeri Barsegov**[1,5,6,*]

[1]Moscow Institute of Physics & Technology, Dolgoprudny, Moscow Region 141700, Russian Federation

[2]Sechenov University, Moscow 119991, Russian Federation

[3]Department of Cell & Developmental Biology, Perelman School of Medicine, University of Pennsylvania, Philadelphia, PA 19104, USA

[4]Institute of Fundamental Medicine and Biology, Kazan Federal University, Kazan 420008, Russian Federation

[5]Department of Chemistry, University of Massachusetts, Lowell, MA 01854, USA

[6]Lead contact

SUMMARY

The space-filling fibrin network is a major part of clots and thrombi formed in blood. Fibrin polymerization starts when fibrinogen, a plasma protein, is proteolytically converted to fibrin, which self-assembles to form double-stranded protofibrils. When reaching a critical length, these intermediate species aggregate laterally to transform into fibers arranged into branched fibrin network. We combined multiscale modeling *in silico* with atomic force microscopy (AFM) imaging to reconstruct complete atomic models of double-stranded fibrin protofibrils with γ-γ crosslinking, A:a and B:b knob-hole bonds, and αC regions—all important structural determinants not resolved crystallographically. Structures of fibrin oligomers and protofibrils containing up to 19 monomers were successfully validated by quantitative comparison with high-resolution AFM images. We characterized the protofibril twisting, bending, kinking, and reversibility of A:a knob-hole bonds, and calculated hydrodynamic parameters of fibrin oligomers. Atomic structures of protofibrils provide a basis to understand mechanisms of early stages of fibrin polymerization.

Graphical Abstract

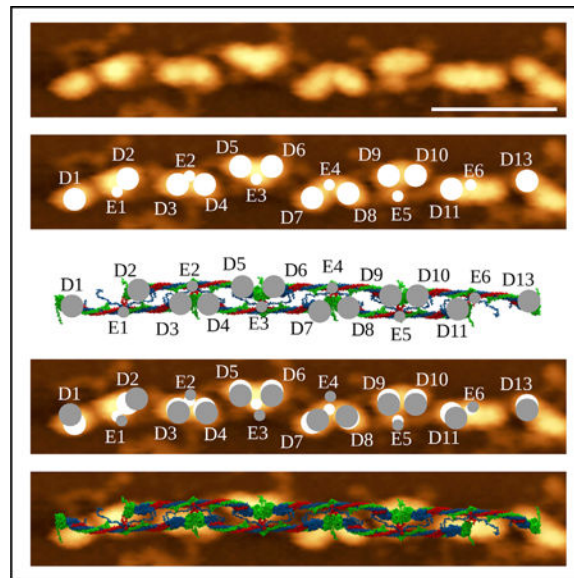*Correspondence: weisel@pennmedicine.upenn.edu (J.W.W.), valeri_barsegov@uml.edu (V.B.).

DECLARATION OF INTERESTS

The authors declare no competing interests.

In Brief

Zhmurov et al. used 27 relevant crystal structures to computationally reconstruct the full-atomic models of fibrin oligomers and protofibrils, which correlate with high-resolution atomic force microscopy images. The structures contain much valuable information for understanding the early stages of fibrin polymerization.

INTRODUCTION

Fibrin is an end product of blood clotting that forms the scaffold of hemostatic clots and obstructive thrombi in blood vessels. Fibrin is also a major component of the extracellular matrix and is involved in a broad range of cellular processes, including cell adhesion, migration, proliferation and differentiation, wound healing, angiogenesis, and inflammation (Weisel and Litvinov, 2017; Litvinov and Weisel, 2017). Fibrin is widely used as a versatile biomaterial in a variety of applications, such as hemostatic sealants, tissue engineering, as a delivery vehicle for cells, drugs, growth factors, and genes, and matrices for cell culturing (Janmey et al., 2009; Radosevich et al., 1997). Because of the fundamental biological and medical importance, molecular mechanisms of fibrin formation as well as fibrin structure and properties continue to be major areas of research (Weisel and Litvinov, 2013, 2017; Litvinov and Weisel, 2016).

Fibrin formation is initiated by the cleavage of fibrinopeptides A and B from the N termini of Aα and Bβ chains of fibrinogen, respectively, to produce fibrin monomer. The release of fibrinopeptides A exposes an N-terminal α-chain motif GPR, called knob ''A'', which binds to constitutively exposed hole ''a'' in the γ nodule of another fibrin molecule (Everse et al., 1998; Kostelansky et al., 2002), resulting in the formation of an A-a knob-hole non-covalent bond (Litvinov et al., 2005). Exposure of knobs ''A'' is necessary and sufficient to form fibrin through the interaction with holes ''a.'' The release of fibrinopeptides B exposes an

N-terminal β-chain motif GHRP, called knob ''B'', which is complementary to hole ''b'' located in the b nodule of another fibrin molecule.

Fibrin polymerization begins when two monomeric fibrin molecules interact in a half-staggered fashion through the A-a knob-hole interaction. The addition of a third molecule is accompanied by an end-to-end association where, in addition to the A-a knob-hole interactions, the globular D regions of two adjacent molecules form the D:D interface. The D:D interface provides a junction between the monomers in one of the two strands in a fibrin trimer. Furthermore, fibrin monomers add longitudinally via the inter-strand A-a knob-hole bond formation and intra-strand D-D interactions to form fibrin oligomers. This growth continues until the fibrin oligomers reach the critical length of protofibrils: oligomers made of ~20–25 fibrin monomers. Fibrin protofibrils self-associate laterally to form twisted fibers of variable thickness. These branches form a three-dimensional fibrin network called a clot (Weisel and Litvinov, 2017).

The monomeric fibrin is essentially identical in structure and composition to fibrinogen except for small fibrinopeptides A and B, which are cleaved when fibrinogen is converted to fibrin, and αC domains, which are bound to the central nodule in fibrinogen but detached in fibrin (Medved et al., 2001). Therefore, fibrin oligomers and protofibrils can be reconstructed using resolved crystal structures of the human fibrinogen molecule and parts of fibrinogen and fibrin molecules, including the fibrinogen fragment D and the double-D fragment from crosslinked fibrin (see Table S1). Yet using the crystal structures of fibrinogen or fibrin [together denoted as fibrin(ogen)] is challenging. First, the crystallographic data available are incomplete. There are several flexible unstructured portions that are not resolved crystallographically yet are essential for fibrin formation, including residues 1–26 and 1–57 at the N-termini of the Aα and Bβ chains, respectively, and residues 201–610, 459–461, and 395–411 at the C-termini of the Aα, Bβ, and γ chains, respectively (Kollman et al., 2009). Second, a manifold of possible spatial arrangements of fibrin monomers when forming a protofibril makes *in silico* reconstruction of fibrin protofibril difficult. Third, the large system size requires using vast computational resources: a 0.5- to 0.6-μm-long protofibril made of 20 fibrin monomers contains ~60,000 amino acids, which corresponds to ~10^6 atoms.

Determination of atomic structures of fibrin oligomers cannot be accomplished by X-ray crystallography and/or electron microscopy, owing to the unstable nature of these heterogeneous intermediate supramolecular assemblies and their characteristic elongated shape. Yet atomic-level information about these structures is necessary to elucidate the mechanisms of formation and properties of fibrin polymers, which provide the three-dimensional scaffold necessary to maintain the integrity and viscoelasticity of blood clots and thrombi. Here we employed multiscale modeling to computationally reconstitute the atomic structures of double-stranded fibrin oligomers of varying length. The atomic structural models were successfully validated using high-resolution atomic force microscopy (AFM) imaging of fibrin oligomers.

We employed the molecular dynamics (MD) simulations of atomic structural models (Brooks et al., 2009; Zhmurov et al., 2012) and C_α-based self-organized polymer (SOP)

models of fibrin(ogen) and its fragments (Hyeon et al., 2006), accelerated on graphics processing units (GPUs) (Zhmurov et al., 2010a, 2010b; 2011; Alekseenko et al., 2016), to perform a step-by-step reconstruction of a complete atomic structure of a 19-monomer-long fibrin protofibril using the recently published structure of a short fibrin oligomer (Zhmurov et al., 2016). The protofibril structure has interesting properties, such as twisting, bending, and kinking, and the presence of free knobs ''B'' necessary for formation of additional intra- and inter-protofibril bonds. The models obtained enabled us to explore the dynamic structural transitions in fibrin protofibrils and to predict experimentally unavailable dynamic characteristics of fibrin oligomers and protofibrils, including density, radius of gyration, diffusion coefficient, and intrinsic viscosity.

RESULTS

Stepwise Reconstruction of Fibrin Oligomers and Protofibril

As a building block, we used the structure of short double- stranded fibrin oligomer $FO_{2/3}$ with two fibrin monomers in the first and three monomers in the second strands (Figure 1A). Using this structure, we performed stepwise elongation to create longer oligomers up to the length of a protofibril. The full-atomic model of $FO_{2/3}$ was constructed computationally in our previous study (Zhmurov et al., 2016) using all 27 relevant crystal structures of fibrinogen and its fragments resolved to date (Table S1). The structure of $FO_{2/3}$ showed good agreement with high-resolution AFM images (Zhmurov et al., 2016). In this work, we took the next step to elongate several-fold the known structure of $FO_{2/3}$ in order to reconstruct longer fibrin oligomers $FO_{m/n}$ (m/n is the number of fibrin monomers in the first/second strand). This enabled us to recreate short fibrin oligomers from $FO_{2/3}$ to $FO_{5/6}$. A mere replication of the $FO_{2/3}$ structure along the longitudinal axis has resulted in formation of elongated oligomers and protofibrils that do not show any twisting detected in experimental AFM and electron microscopy images (Weisel et al., 1987; Medved et al., 1990; Protopopova et al., 2015; Huang et al., 2014). To overcome this problem, we designed an approach that uses two main crystal structures of the D:D junction. These structures correspond to the straight conformation (PDB: 1N86) of the D:D interface, used to recreate shorter fibrin oligomers, and the bent conformation (PDB: 1FZG) of the D:D interface, which we used to recreate longer oligomers (and a protofibril). To recreate twisted structures, we align two $FO_{2/3}$ constructs using the straight conformation of D-D junctions and then gradually switch to the bent conformation of the D:D junction (STAR Methods). This builds in the desired twist in the fibrin strands, in full agreement with AFM and electron microscopy experiments (Protopopova et al., 2015; Weisel et al., 1987).

A step-by-step reconstruction of short fibrin oligomers ($FO_{m/n}$) is illustrated in Figure 1B (elongation step with the straight conformation of D:D interface). Reconstruction of longer fibrin oligomers and protofibril ($FP_{9/10}$) is illustrated in Figure 1C (a procedure to introduce a twist; bent conformation of D:D interface; see also STAR Methods for more details). In step A of the twisting procedure, coarse-graining of $FO_{2/3}$ is performed (diamonds in Figure 1B) and Langevin simulations of the C_α-based representation of $FO_{2/3}$ is carried out to switch from the straight to the bent configuration of the D:D interfaces. In step B of the twisting procedure, the obtained conformation of $FO_{2/3}$ is back-mapped and energy-

minimized using the all-atom solvent-accessible surface area model of implicit solvation. Next, we perform the elongation procedure. The atomic model of $FO_{2/3}$ with knobs ''A'' and ''B'' is replicated to reconstruct fibrin oligomers ($FO_{n/m}$) of the desired length. In the last structure-addition step, the αC regions are incorporated into each fibrin monomer, and the covalent γ-γ crosslinks between residues γ398 and γ406 of abutted fibrin monomers are introduced (Rosenfeld et al., 2015). The final structures of double-stranded fibrin polymers from the structure-addition step (Table 1) were energy-minimized to exclude possible steric clashes.

Atomic Structures and AFM Images of Fibrin Oligomers and Protofibrils

To compare *in silico* structures with AFM images, we employed the computational Monte Carlo procedure, which overlaps the positions of the centers of mass of D and E regions in the atomic structural model and in AFM images (see STAR Methods and Figure 2B). To quantify the agreement between AFM images and atomic models, we monitored the dynamics of total root-mean-square deviation (RMSD) in Monte Carlo runs. The trajectories in Figure 2C show a great reduction in RMSD values to 0.9–2 nm depending on the oligomer length.

We first recreated atomic models of short fibrin oligomers by applying the elongation procedure (Figure 1B) to the initial structure of $FO_{2/3}$, to reconstruct the structures up to nine monomers long (FO4/5, Figure 2A). We correlated these structures with their high-resolution AFM images for short oligomers containing up to nine fibrin monomers ($FO_{4/5}$; Table 1). In AFM imaging, short fibrin oligomers appear as elongated constructs with regularly spaced heart-shaped nodules and two adjacent nodules facing in opposite directions (Figure 2). Each of these nodules corresponds to a single D-E-D trinodular unit. The derived atomic structures and AFM images for short fibrin oligomers are compared in Figures 2B and 2D, which show good agreement between the structures obtained experimentally and computationally. Next, we turned to reconstruction of longer oligomers ($FO_{5/6}$ and longer) up to a protofibril $FP_{9/10}$. We elongated oligomer $FO_{4/5}$ with $FO_{2/3}$ using the elongation procedure described in the STAR Methods (Figure 1B). The structures obtained *in silico* did not compare well with their corresponding AFM images (Figures 2E and 3F), which could be due to protofibril twisting not present in the modeled structures. Quantitatively, this is reflected in higher values of RMSD for longer structures (0.9–1.0 nm for short oligomer $FO_{3/3}$ versus 1.8–2.0 nm for long oligomer $FO_{6/7}$; see Figure 2C). Next, we elongated short oligomers up to the length of a fibrin protofibril $FP_{9/10}$ (Figure 3A and Table 1). At this length scale, the structure of $FP_{9/10}$ obtained with the straight conformation of D:D interface did not capture the helical twist observed in AFM images (Figures 2E, 2F, and 3D). Using the structure of $FP_{9/10}$ obtained computationally, we calculated the helical radius and helical pitch, which came to 650 nm and 3,300 nm, respectively. This is a straight structure on the protofibril length scale of ~500 nm.

To build in a twist in fibrin oligomers and protofibrils, we first applied the twisting procedure (Figure 1C) and then the elongation procedure (Figure 1B). The equilibrium structure obtained shows that the transition from the straight to the bent double-D conformation with the twisting procedure results in an overall shape change of $FP_{9/10}$ from

the parallel double-stranded (Figure 3A) to the twisted (double-stranded) helical form (Figure 3B). Transient structures of $FP_{9/10}$ populated in the course D:D interface remodeling are displayed in Figure S2 (see Video S1). As the protofibril $FP_{9/10}$ twists, the helical radius and helical pitch decreases, respectively, from 650 nm to 5 nm and from 3,300 nm to 400 nm (see Figure S2 and Video S1), as a result of dynamic remodeling of all D:E:D interfaces reinforcing the protofibril's structure. The comparison of atomic structures and AFM images of longer fibrin oligomers showed better agreement (Figure 3D). Note that the average values for RMSD are slightly lower for twisted structures (1.2 ± 0.3 nm; sample size = 30) compared with straight oligomers (1.4 ± 0.4 nm; sample size = 30).

Complete Structure of a Fibrin Protofibril with the αC Regions

The C-terminal part of fibrinogen's Aα chain, called the αC region (residues Aα221–610), consists of the proline-rich unstructured αC connector (Aα221–390) and the relatively compact αC domain (Aα391–610) (Tsurupa et al., 2009). The αC region is missing in all the crystal structures of fibrinogen and its fragments resolved to date. The structure of bovine fibrinogen's αC domain was partially resolved by nuclear magnetic resonance (Burton et al., 2007), yet the structure of human fibrinogen's αC domain is not known (Tsurupa et al., 2009). We recreated this structure using sequence homology between the human and bovine fibrin(ogen) with the Modeller software suite (Webb and Šali, 2017). Structure snapshots of the αC domain randomly selected from independent MD runs showed a double β hairpin stabilized by the S-S bond. The αC-domains can be separated into the N-terminal and C-terminal subdomains as suggested earlier (Tsurupa et al., 2009, 2012). Since αC connectors are not resolved by the X-ray crystallography, they do not possess stable secondary or tertiary structure. Therefore, the incorporation of αC connectors in a random coil conformation does not lead to any structural artifacts. In a structure-addition procedure (Figure 1D), we incorporated the missing C-terminal portions of the α connector in a random conformation to arrive at the complete atomic structure of a fibrin protofibril $FP_{9/10}$ (Figure 3C).

We compared the full-atomic structure of $FP_{9/10}$ containing αC regions with the AFM images (Figure 3). The protofibril's shape and positions of the αC regions in the atomic model and AFM images of $FP_{9/10}$ agreed well. The αC regions were predominantly perpendicular to the protofibril axis. Although the αC regions were occasionally interconnected, they were mostly single. Not all αC regions were seen in AFM images (assuming two αC regions per monomer), and we identified on average 1.6 αC regions per monomer. Some of the αC regions might have been proteolytically truncated in the fibrinogen purified from plasma or have been adsorbed at positions not clearly visible on the surface (e.g., under the protofibril backbone).

Conformational Dynamics of the Fibrin Protofibril Chain

From experimental AFM images, the average contour length of fibrin protofibrils is 213 ± 101 nm and the average end-to-end distance is 197 ± 86 nm (n = 30). This gives an average end-to-end to contour length ratio of 0.94 ± 0.09 (n = 30), which shows that protofibrils are bent. Since our *in silico* structures were recreated based on the X-ray data, they lack this conformational flexibility. To explore dynamic transitions in the protofibril

structure, we performed MD simulations using the obtained structure of $FP_{9/10}$ (see STAR Methods and Video S2), which revealed significant structural alterations including bending (Figure 4A) and kinking (Figure 4B). This agrees well with the previously published experimental data (Protopopova et al., 2015, 2017; Huang et al., 2014; Chernysh et al., 2011; Medved et al., 1990; Hunziker et al., 1988; Fowler et al., 1981) and with our AFM images (Figure 4).

The distribution of end-to-end distances (i.e., the distances between centers of the end D:E:D complexes) in $FP_{9/10}$ from MD simulations is displayed in Figure 4F. The average end-to-end distance in $FP_{9/10}$ is $R = 330 \pm 15$ nm. With the contour length $L_0 = 403$ nm (9 monomers, 44.8-nm length of monomer), the average persistence length of protofibril $FP_{9/10}$ is $L_p = 320 \pm 80$ nm (see STAR Methods). There is a variation in experimental estimates of L_p for fibrin protofibrils, with values ranging from ~100 nm to 500 nm (Piechocka et al., 2016; Storm et al., 2005). Based on our AFM images, $L_p = 420$–480 nm, which is in good agreement with our simulations. The higher value of L_p observed in AFM images can be attributed to the non-covalent interactions (adsorption forces) between the protofibrils' backbone and the surface. Reversible formation of kinks in the protofibril structure observed in our simulations was due to simultaneous bending of the coiled coils in adjacent strands around the positions identified in the previous simulation studies (Köhler et al., 2015; Figure 3). This is in agreement with AFM images, in which kinks were indeed detected (Figure 4E). Deviations of the atomic structures from the AFM images at the protofibril's tails are due to limited sampling of the conformational space in the MD simulations. The probability distribution of kinking angles from MD simulations for $FP_{9/10}$ is shown in Figure 4G.

To quantitatively compare the AFM images and the atomic structural models, we computed the distributions of distances between adjacent D regions (Figure 4H), distribution of distances between D and E regions in DED constructs (Figure 4I), and distribution of distances between DED complexes (Figure 4J). To probe the bending rigidity of protofibrils, we computed the distributions of angles formed by three DED complexes (Figure 4K). To extract these characteristics from AFM images, we only selected protofibrils in which these fragments are visible and located their geometric centers; in the simulations, we computed the centers of mass of these fragments. The average values of all four quantities from AFM images and equilibrium MD simulations agree well (see Table S2), although SDs are larger in AFM images.

Structural Transitions in Fibrin Protofibril

Dissociation of A:a Knob-Hole Bonds—The long 10-ms MD simulations of $FP_{9/10}$ showed that the A:a knob-hole bonds dissociate. This significantly weakens the D:E:D interface, leading to disruption of the D:D junction (Figure 4C), which does not occur when the A:a knob-hole bonds are intact. The D:D junction is the weakest link in the single-stranded fibrin oligomers (Zhmurov et al., 2011, 2012). In accord with these findings, AFM images also show irregularly shaped D:E:D fragments, which suggests the D:D interface disruption (see Figures 2E, 2F, 3E, 4D, and 4E). These results point to the importance of γ-γ covalent crosslinking, which reinforces the D:D interface when fibrin protofibrils form.

αC Regions—To sample conformations of the αC regions with flexible βN regions, we performed 10-ms equilibrium MD simulations of the protofibril FP$_{9/10}$ with a constrained protofibril backbone and free knobs ''B'' (STAR Methods; see Video S3). We constructed the probability distribution of the distances between the protofibril longitudinal axis and the centers of mass of αC domains and compared it with the experimental histogram of the same quantity. Figure 5B shows that the agreement is very good, albeit the SDs are smaller in the simulations. This might be due to overstabilization of the αC domains in the simulations. The structure of the αC domain is not resolved experimentally, which suggests that it is not stable. Longer αC connectors are typically bent, which explains why the average distance between the αC regions and the protofibril backbone is only 17 nm (Figure 5B).

B:b Knob-Hole Interactions—We explored the conformational transitions in the βN regions with knobs ''B.'' The GHR active sequence does not drift far away from the central nodule, making the intra-protofibril B:b highly unlikely to form (Figure 5E). This suggests that additional structural changes in the protofibril are required for the B:b knob-hole bonds to form within the protofibril, in full agreement with earlier reports (Medved et al., 2001). These transitions (B:b knob-hole bond formation) cannot be sampled in MD simulations due to the limited time span (10 ms), and there might be additional putative inter-atomic contacts that guide the βN re gions toward the holes ''b.'' There is experimental evidence suggesting that the B:b knob-hole bonds can form both between the fibrin strands inside the protofibril and between the protofibrils (Litvinov et al., 2007; Blombäck et al., 1978; Weisel, 1986). For this reason, we recreated two protofibril constructs: one with knobs ''B'' bound to holes ''b,'' and the other with free knobs ''B''; see the PDB files in Data S1 for knobs-in structure and Data S2 for knobs-out structure.

Hydrodynamic Parameters of Fibrin Oligomers and Protofibril—We calculated the (hydro)dynamic molecular characteristics for double-stranded fibrin oligomers and protofibrils (STAR Methods) and profiled them as a function of their size (Figure 6 and Table 1). First, we compared our theoretical predictions with available experimental values for some of these quantities. Very good agreement was found for the (translational) diffusion coefficient D, i.e., $(1.5–2.2) \times 10^{-7}$ cm^2/s (experiment for full-length fibrinogen; Raynal et al., 2013) versus $(2.5 \pm 0.3) \times 10^{-7}$ cm^2/s (our simulations for truncated fibrin monomer without αC regions). Slightly lower values of D obtained for the full-length fibrin monomer can be attributed to the presence of bulky αC appendages, which are absent in truncated fibrin variants. Using confocal microscopy, Chernysh et al. (2011) estimated the diffusion coefficient (D) for 500-nm-long protofibril to be $D = 3.7 \times 10^{-8}$ cm^2/s. This is in very good agreement with our values for FP$_{9/10}$, i.e., $D = (3.4 \pm 0.2)$ 3 10^{-8} cm^2/s for the full-length molecules and $D = (4.0 \pm 0.1) \times 10^{-8}$ cm^2/s for those with truncated αC region (Table 1). Given these values of the diffusion coefficient the time needed for the protofibrils to travel toward one another will be fractions of a second, which is significantly shorter than overall polymerization timescale of minutes under similar conditions (Protopopova et al., 2017). Thus, the lateral aggregation of protofibrils is not limited by their diffusion.

The density of fibrin oligomers (1.34–1.36 g/cm^3) was also found to be in good agreement with experiments ($\rho = 1.38$ g/cm^3; Adamczyk et al., 2012). The density of fibrin with flexible αC regions (1.32–1.33 g/cm^3) was lower than the density of fibrin without αC regions (1.34–1.36 g/cm^3). Theoretical values of the intrinsic viscosity η for the truncated fibrin (24 ± 9 cm^3/g) and full-length fibrin monomer (38 ± 19 cm^3/g) are also within the experimental range (21–48 cm^3/g; Adamczyk et al., 2012). Larger variability in the theoretical values of η for the full-length fibrinogen is due to higher extensibility of αC appendages (Table 1). This supports our findings, namely that fibrinogen in solution exists in two conformational populations: one population with a lower value of η corresponding to conformations of fibrin's αC domains attached to the central nodule; and the other population with a higher value of η that corresponds to conformations with free αC regions (Zuev et al., 2017). The agreement between experimental and theoretical values of D, ρ, and η we have obtained for fibrin monomers and the structures we have recreated enabled us to predict the values of D, ρ, and η and radius of gyration R_g for fibrin oligomers and protofibrils not available experimentally (Table 1). We also derived analytical expressions that allow for the extrapolation of these quantities to fibrin protofibrils of arbitrary length (Figure 6).

DISCUSSION

Fibrin oligomers and protofibrils are important intermediate products formed early during fibrin polymerization. Resolution of atomic structures of fibrin oligomers and protofibrils is needed to illuminate the mechanisms of the early stages of fibrin formation, including lateral aggregation of protofibrils, and to characterize the remarkable extensibility and viscoelasticity of fibrin fibers (Liu et al., 2010; Litvinov and Weisel, 2017). Yet experimental determination of the structure and characterization of the properties of double-stranded fibrin polymers is difficult due to their elongated shape and highly unstable nature. We employed a powerful combination of the state-of-the-art experimental AFM imaging technique and theoretical approaches to multiscale modeling accelerated on a GPU to gather the atomic-level information about the structure and properties of fibrin oligomers and protofibrils. Using the full-atomic structure of a short fibrin oligomer FO$_{2/3}$ (Figure 1; Zhmurov et al., 2016), here we have reconstructed the atomic structures of longer fibrin oligomers FO$_{3/4}$–FO$_{7/8}$ up to a 19-mer protofibril FP$_{9/10}$ (Figures 2 and 3; Table 1). These constructs involve γ-γ crosslinking, A:a and B:b knob-hole bonds, and αC regions—all important functional elements of fibrin—and carbohydrates. The double-stranded fibrin structures were successfully validated through the direct comparison with high-resolution AFM images of oligomers and protofibrils (Figures 2 and 3; Data S1 and S2).

Early products of fibrin polymerization are two-stranded oligomers (Fowler et al., 1981; Chernysh et al., 2011; Huang et al., 2014). A common feature of fibrin oligomers visualized with transmission electron microscopy is their twisted helical shape, although reported parameters of the oligomers' helicity are highly variable. Medved et al. (1990) showed that some protofibrils form twisted structures with a helical pitch of ~100 nm, whereas other protofibrils are nearly straight. In agreement with this study, we found that the helical pitch decreases from 3,300 nm to 400 nm (Figure 3) following the transition from the straight conformation (PDB: 1N86) to the bent conformation (PDB: 1FZG) of the D:D interface

(Figures 3A, 3B, and S2), and the helical radius decreases from 650 nm to 5 nm. This points to the important role played by the D:D interfacial flexibility in early stages of fibrin polymerization. We did not observe a helical pitch <400 nm, which might be due to the experimental conditions used in previous studies (Medved et al., 1990) or to crystal packing forces in the atomic structures used. In most experiments, fibrin protofibrils are straight and thin, which agrees with our results. After reaching a certain length, fibrin protofibrils aggregate laterally to form thick twisted fibers. Fibrin fibers have a 20- to 60-nm helical radius and ~2,000-nm helical pitch (Weisel et al., 1987), and continue to twist as they grow.

The reconstructed double-stranded fibrin oligomers and protofibrils correspond to the known ultrastructures, but surpass the available experimental data in spatial resolution. We are aware of other models of fibrin protofibrils (Yang et al., 2000; Pechik et al., 2006; Huang et al., 2014). The model proposed by Yang et al. (2000) captures the main structural features of fibrin oligomers, including the half-staggered molecular overlay formed by two fibrin strands. However, this model is ad hoc rather than systematic, and lacks a detailed analysis of the crystal forms. This model provides a static view of fibrin structure with missing γ-γ crosslinking, A:a and B:b knob-hole bonds, and αC regions. Another model (Huang et al., 2014) captures the half-staggered molecular arrangement of fibrin strands, and has a helical pitch of 90 nm. Yet a closer look reveals major steric clashes in the DED regions, which make the A-a bond formation unlikely. Also, this model is lacking γ-γ crosslinking, knob-hole bonds, and αC regions, and is based on the chicken fibrinogen structure (PDB: 1M1J).

We employed equilibrium MD simulations of fibrin protofibril FP$_{9/10}$ to explore the dynamic structural transitions that occur in double-stranded fibrin polymers. Fibrin protofibrils behave like other double-stranded biopolymers, such as double- stranded DNA, but with a longer 320-nm persistence length, and show a high degree of bending. A theoretical probability density curve shows that due to bending, the end-to-end distance in FP$_{9/10}$ decreases from ~400 nm (contour length) to ~330 nm (Figure 4F). This might be important for the fiber formation and fiber branching (Figure 4). Experimental AFM images reveal more bending flexibility than the *in silico* structures, and the protofibril's bending becomes more pronounced with increasing length. We also observe reversible kinking of the protofibril backbone with the 80° to 140° kinking angle range and an average kinking angle of 115° (Figure 4G). Protofibril bending and kinking could be one of the mechanisms of initiation of branch points in growing fibrin fibers.

In the simulations, we observed the dissociation of A:a knob-hole non-covalent bonds, which was followed by the disruption of the D:E:D interface. This suggests a secondary role played by the D:D interface in fibrin polymerization, and also potentially supports the so-called Y-ladder model of fibrin fiber growth (Rocco et al., 2014). According to this model, the D:E:D interface becomes stable only after both knobs ''A'' are bound to their corresponding holes ''a'' (Rocco et al., 2014). Since upon the disruption of D:E:D interface and D-region rotation one A:a knob-hole bond is completely dissociated, a knob ''A'' and a hole ''a'' might become available for inter-protofibril cross-coupling. Another fibrin monomer from another protofibril could then bind, thus initiating a branch point. Formation of branch points is visible in some of the protofibril images (Figure 4E). We did not observe

formation of new A:a knob-hole bonds in the millisecond timescale of simulations, hence this transition occurs in a longer timescale.

The length of αC connectors is very important for mechanical properties of fibrin fibers (Falvo et al., 2008). Since the αC domains are capable of interacting with each other (Tsurupa et al., 2011, 2012; Litvinov et al., 2007) and with the globular parts of fibrin molecules (Tsurupa et al., 2009), it is important that they have an optimal length. When the αC connectors are long (as in human fibrinogen) their αC domains tend to form non-covalent bonds with other αC domains within the same protofibril and between the protofibrils. When the αC connectors are short (as in chicken fibrinogen), the αC domains hardly form binding contacts between protofibrils but only within the protofibril. We see in the simulations and in AFM images that the span of the αC regions is long enough so that the αC domains can form the αC-αC contacts within the protofibril and between protofibrils (Figure 5). The experimental histogram of the lengths of αC region shows the 10- to 35-nm range and an average length of 17.3 nm; the theoretical probability density curve reveals a smaller 10- to 20-nm range and a similar average length of 14.7 nm. This large variability also explains why in AFM images were on average 1.6 αC regions per fibrin monomer (<2). Our results imply that the conformational dynamics of αC regions plays a role in defining the thickness of fibrin fibers (number of protofibrils in a fiber).

The physiological role of B:b knob-hole bonds is not yet fully understood (Weisel and Litvinov, 2017). Although knobs ''B'' are long enough to reach and bind to the corresponding holes ''b'' in the same protofibril, our simulations of $FP_{9/10}$ with free knobs ''B'' show that they have a limited span due to thermal fluctuations (Figure 5E). Hence, formation of intra-protofibril B:b contacts is possible only when Nβ regions are close to the globular parts of fibrin, interacting with γ and β nodules of adjacent molecules (Moskowitz and Budzynski, 1994). These interactions can guide the knob ''B'' to the hole ''b'' or/and to the thrombin active-site cleft (Pechik et al., 2006). Upon formation of B:b knob-hole bonds, the β nodule dissociates from the a-helical coiled coil, which results in the exposure of the tissue plasminogen activator and plasminogen binding cites in the coiled coil (Medved et al., 2001). This transition might help to bring holes ''b'' of adjacent protofibril closer to knobs ''B,'' thus facilitating the inter-protofibril contacts' formation. Our simulations for protofibril $FP_{9/10}$ suggest that the intra-protofibril B:b contacts are less probable than the inter-protofibril B:b contacts, which also explains why the formation of fibrin fibers occurs even in the absence of knobs ''B'' (Moskowitz and Budzynski, 1994; Weisel, 1986).

We calculated the molecular hydrodynamic parameters for double-stranded fibrin oligomers and protofibrils, which are not available experimentally (Table 1), and extracted the scaling laws for R_g, D, η, and ρ as functions of their size N (number of fibrin monomers; Figure 6). The protein density ρ was found to depend on N exponentially (Figure 6C) in full agreement with the predictions made by Fischer et al. (2004). The profile of R_g shows a linear increase with N starting from 5 to 7 monomers (Figure 6A), because at larger N fibrin oligomers are pseudo-one-dimensional with size growing with N. This also explains why the intrinsic viscosity η increases quadratically with N. According to the Flory theory, $\eta = \Phi R_g^3/M$,

where Φ is a universal constant and M is the molar mass (Doi and Edwards, 1986). Indeed, for a linear polymer $R_g \sim N$ and $M \sim N$, and so $\eta \sim N^2$ (Figure 6D).

STAR★METHODS

KEY RESOURCES TABLE

CONTACT FOR REAGENT AND RESOURCE SHARING

Further information and requests for resources and reagents should be directed to and will be fulfilled by the Lead Contact, Valeri Barsegov (Valeri_Barsegov@uml.edu).

EXPERIMENTAL MODEL AND SUBJECT DETAILS

Not applicable.

METHODS DETAILS

Preparation of Fibrin Oligomers and Protofibrils—0.15 mg/ml human fibrinogen (Hyphen BioMed, France) in 20 mM Tris-HCl buffer (pH 7.4) containing 150 mM NaCl and 10 mM $CaCl_2$ was mixed with 0.05 U/ml thrombin (final concentration), incubated for 5 min at room temperature, and then diluted 100-fold with buffer and immediately used in AFM sample preparation.

Atomic Force Microscopy—AFM imaging was performed on the surface of modified hydrophilized graphite (Protopopova et al., 2015). 3 μl of a sample solution was applied on the modified graphite surface and kept for 15 s at room temperature. A ~50x volume drop of fresh milli-Q water was then carefully placed above the sample solution for 10 s and then removed with a flow of air making the surface ready for imaging. The AFM imaging was performed using a MFP-3D microscope (Asylum Research - Oxford Instruments, USA) in AC mode with a typical scan rate of 0.8 Hz. Images were taken in air using super-sharp cantilevers with a tip radius about 1 nm (Klinov et al., 1998). Femto-Scan software (http://www.femtoscanonline.com) was used to filter and analyze the AFM data.

Elongation Step—We recreated fibrin protofibrils $FP_{n/m}$ by replicating the structure of oligomer $FO_{2/3}$. A schematic of elongation procedure is displayed in Figure S1. First, we removed two fibrin molecules from the atomic model of $FO_{2/3}$ that leaves only one half-molecule overlap (two far-most molecules in Figures 1 and S1) to obtain the structure of $FO_{1/2}$. Next, we aligned two copies of $FO_{1/2}$ so that one monomer in the upper strand of the first copy overlaps with another monomer of the second copy (Figure S1) to obtain the structure of oligomer $FO_{2/3}$. This step was repeated using fragments $FO_{2/3}$ and $FO_{1/2}$ placed at the growing end of fibrin polymer to obtain the structures of desired length $FO_{n/m}$.

Twisting Procedure—*Step A. $FO_{2/3}$ structure refinement and energy minimization*: Initial reconstruction of $FO_{2/3}$ oligomer obtained in our previous study (Zhmurov et al., 2016) was based on the PDB structure 1N86. This structure corresponds to the straight conformation of the D:D interface. We utilized the SOP-GPU package (Zhmurov et al., 2010a; 2010b) to carry out the Langevin dynamics simulations of the C_α-based SOP model

of $FO_{2/3}$ with side chains to induce structural rearrangements in $FO_{2/3}$ due to the D:D interface transitioning from the straight conformation to the bent conformation. We ''switched off'' the binding interactions reinforcing the straight double-D structure 1N86 and ''switched on'' the interactions corresponding to the bent double-D structure 1FZG. We used the positions of C_α- and C_β-atoms taken from the published $F_{O2/3}$ structure (Zhmurov et al., 2016). To parameterize the SOP model of $FO_{2/3}$, we used structures 3GHG, 1N86 and 1FZG. Parameters for the knob-hole interactions were taken from the structure of fibrinogen 3GHG co-crystalized with peptides GPRP and GHRP. *Step A* was considered to be complete when the number of native contacts, potential energy of the polypeptide chain, helical pitch and helical radius of $FO_{2/3}$ all leveled off, attaining some constant values. *Step B. Recreating the atomistic structure of fragment $FO_{2/3}$*: Back-mapping of the atomic structure of $FO_{2/3}$ from its coarse-grained counterpart was achieved through the initial placement of atoms and subsequent structure refinement using energy minimization (Wassenaar et al., 2014). Next, we performed energy minimization with harmonic constraints applied to all C_α-atoms. These constraints were imposed using the C_α-atoms positions in the coarse-grained structure from *Step A*. Gradient descent energy minimization was used with the spring constants for constrained atoms gradually increasing from 0 to 100 pN/nm. We verified that the positions of all C_α-atoms in the full-atomic model coincide with those from the coarse-grained structure with RMSD values < 0.02 nm. The obtained structure was then energy-minimized again using the steepest descent algorithm but now without the constraints.

Structure-Addition Step—In the structures $FO_{n/m}$ there are steric clashes involving atoms of the two newly placed fibrin molecules in the elongation step, there are no γ-γ crosslinks, and there are no αC-regions. In the structure-addition step, steric clashes were removed, and the γ-γ cross-links, αC-regions, and carbohydrates were incorporated into the fibrin oligomers $FO_{n/m}$ and protofibril $FP_{9/10}$. The αC regions with disordered part (residues 210–391) and ordered part (residues 392–610) were recreated using the Modeller software (Webb and Šali, 2017). Energy minimization of complete structures $FO_{n/m}$ and $FP_{9/10}$ was performed in the full-atomic resolution. To visualize the structural transitions in a protofibril that correspond to the transformation from the straight to the bent D:D self-association interface, we applied the elongation procedure to the initial and transient structures (see Figures 2 and S2; see also Video S1).

Comparison of the AFM Images with Atomic Structural Models—To compare the atomic structures with AFM images, we developed a procedure based on Monte Carlo simulations. First, we take an AFM image and locate geometric centers of D and E regions (white circles in Figure 2B). Next, we take an *in silico* structure of the same length and reduce it to the centers of mass of the D and E regions (grey circles in Figure 2B). Then, a rigid-body translation/rotation Monte Carlo step is made using the positions of the globular regions in an *in silico* structure. The step is accepted if the total RMSD value for distances between the globular regions in an AFM image and the atomic structure is reduced; otherwise the step is rejected. The translation/rotation amplitude is randomly selected from the 200-nm interval for translations and 180-degree interval for rotations. If 100 sequential translational/rotational steps are rejected, then the amplitude of translational-rotational steps is reduced by 5%. The Monte Carlo simulation is considered to be complete when the

amplitudes for translations and rotations reach the threshold value (0.01 nm for translations and 0.01 degrees for rotations). Finally, the total translational-rotational transformation is applied to the full-atomic structure of fibrin oligomer (back-mapping; see Figure 2B). We performed a total of 20 Monte Carlo runs for each AFM image, from which we then selected the image with the lowest total RMSD. The dynamics of RMSD values for the AFM images of fibrin oligomers displayed in Figure 2 are in Figure 2C, which shows higher RMSD values for longer oligomers and lower RMSD values for twisted vs. straight oligomers (i.e. 1.2 ± 0.3 nm vs. 1.4 ± 0.4 nm; sample size = 30).

Conformational Dynamics of Fibrin Protofibril—We performed coarse-grained modeling of $FP_{9/10}$ with SOP force field (Zhmurov et al., 2011). To speed up conformational sampling, we used the under-damped Langevin simulations in the low friction limit. We set $\varepsilon_h = 0.7$ kcal/mol for all residue-residue contacts stabilizing the native state of $FP_{9/10}$. Equilibrium contact distances for the intra-monomer contacts were taken from the crystal structure of fibrinogen (PDB structure 3GHG) and for contacts between knobs 'A' and holes 'a' or selected structures of the D:D interface (PDB structure 1FZG). The contacts formed by knobs 'A' were limited to the contacts formed by the active sequence GPR present in the crystal structure of full fibrin(ogen) as a part of GPRP peptide (PDB structure 3GHG). The βN-domains with knobs 'B' were incorporated in random coil conformation and were not inserted into holes 'b'. We performed five 10-ms simulations to explore the conformational transitions in a protofibril $FP_{9/10}$, and pilot simulation with the protofibril backbone constrained to explore the span of αC regions and knobs 'B'.

Structures of αC-region—The αC-connectors were added to the protofibril structure in the extended conformation. The structure of αC-domains (residues Aα392–610) was constructed with Modeller (Webb and Šali, 2017) using sequence homology with the structure of bovine αC-domain (PDB code: 2JOR; Burton et al., 2007). The αC-domain constructs were used as initial structures in all-atom MD simulations. We minimized the energy of αC-domains using the steepest descent algorithm (Brooks et al., 2009), heated αC-domains to 300K, and equilibrated the obtained structures of αC-domains for 1 ms. We randomly selected the structures of αC-domains from the last 500-ns portion of equilibrium simulations and incorporated them into the structure of PF10/9 (38 structures of αC-domain were added to 19 fibrin monomers to construct $PF_{10/9}$). Residues Aα392 were connected to the last resolved residue Aα201 in fibrin(ogen) structure 3GHG using random coil conformations of αC-connectors. In coarse-grained modeling, the structures of αC-domains were stabilized by native contacts identified with Modeller; the αC-connectors were assumed to be unstructured.

Calculation of Persistence Length—The persistence length of fibrin protofibril L_p was computed using the output from equilibrium simulations and the worm-like chain formula for the end-to-end distance (R) fluctuations: $R^2 = 2L_p L_0 \left[1 - \frac{L_p}{L_0} \left(1 - exp \left[-\frac{L_0}{L_p} \right] \right) \right]$, where L_0 is the protofibril contour length (Rubinstein and Colby, 2003). We used the first and last D:E:D constructs separated by the contour length of 9 fibrin monomers ($L_0 \approx 9 \times 44.8$ nm ≈ 403 nm).

Hydrodynamic Parameters—We used the structures from equilibrium MD simulations of fibrin oligomers and protofibrils. For each oligomer and protofibril, we randomly selected 20 structures to calculate the molar mass M; radius of gyration R_g; translational diffusion coefficient D; protein density ρ; and intrinsic viscosity η (Table 1) using HYDROPRO package (Ortega et al., 2011) and US-SOMO package (Rai et l., 2005). Both packages gave very similar results.

All-Atom MD Simulations—We employed the Solvent Accessible Surface Area (SASA) model of implicit solvation based on CHARMM19 force-field. In the SASA model, the mean solvation energy $\Delta G_{solv}(r)$ is proportional to the solvent accessible surface area (SASA) of a solute molecule: $\Delta G_{solv}(r) = \sum_{i=1}^{N} \sigma_i A_i(r)$, where σ_i is the atomic solvation parameter and $A_i(r)$ is the SASA for the i-th atom (Ferrara et al., 2002).

Coarse-Graining with Self Organized Polymer (SOP) Model—We employed the native topology-based SOP model of a polypeptide chain (Hyeon et al., 2006), which have been extensively used in the exploration of proteins (Zhmurov et al., 2010a; 2010b; 2011; Alekseenko et al., 2016), to describe the fibrin structure at a residue-based level of detail (energy minimization at Step A in Figure 1C and structural conformations sampling for fibrin protofibril). In this model, each amino acid residue is represented by two interaction centers: for the backbone part (C_α-atom), and for the side-chain (C_β-atom). Hence, a polypeptide chain is replaced by a collection of the C_α-C_α and the C_α-C_β covalent bonds. The positions of the side-chain atoms are selected for each of 20 different amino acids as follows: (i) there is no side-chain for Gly; (ii) for the aliphatic amino acids (Ala, Val, Leu, and Ile), the C_β-bead is placed at the position of the center of mass of the side-chain; (iii) for residues Thr and Ser, the C_β atom is placed at the position of the hydroxyl oxygen; (iv) the side-chain of the acidic amino acids (Asp and Glu) is placed at the center of mass of the COO^- group; (v) the side-chain of the basic amino acids (Lys and Arg) is placed at the center of mass of the NH_3^+-group; (vi) for Asn and Gln, the C_β-atom is placed at the position of the center of mass of the group CO-NH_2; (vii) aromatic side-chains in Phe and Tyr are represented by the single C_β-bead placed at the geometrical center of the rings (for Tyr, the bead representing the OH-group is also added); (viii) the Trp side-chain having a double-ring structure is represented by two beads placed in the geometrical centers of the rings; (ix) His is represented by a single bead placed at the geometrical center of the five-member ring forming the side-chain; (x) sulfur-containing amino acids (Met, Cys) are represented by the side-chain bead, placed at the position of the sulfur atom; and (xi) the C_γ-atom in Pro is represented by the C_β-bead linked to its C_α-atom and to the C_α-atom of the residue before (thus, forming a cyclic bond structure). The carbohydrate moieties are represented by a set of beads each located at the center of a five-member ring and by peripheral beads for heavy side-chain groups.

SOP Force Field—The potential energy function of the protein conformation U_{SOP} in terms of the coordinates of C_α- and C_β-atoms $\{r_i\} = r_1, r_2, \ldots, r_N$ (N is the total number of beads) is given by $U_{SOP} = U_{FENE} + U_{ANG} + U_{NB}^{ATT} + U_{NB}^{REP}$, where specified the first term is the finite extensible nonlinear elastic (FENE) potential

$$U_{FENE} = -\sum_{b=1}^{B} \frac{k}{2} R_0^2 \log\left(1 - \frac{\left(r_b - r_b^0\right)^2}{R_0^2}\right)$$ with the spring constant $k = 14$ N/m and the

tolerance for the change of a covalent bond distance $R_0 = 2$ Å. In *UFENE*, the summation is performed over all the covalently linked beads (C_α- and/or C_β-atoms), B is a total number of covalent bonds in the system, r_b is the distance between the covalently linked atoms, and r_b^0 is the corresponding equilibrium distance from the energy-minimized full-atomic structure. The following beads are linked covalently: (i) all C_α-atoms along the polypeptide chain forming the backbone; (ii) C_α- and C_β-atoms of the same amino-acid; (iii) C_β-atoms and C_α-atom in the previous residue in Pro; (iv) C_β-atoms in Cys residues forming a mutual disulfide bond; and (v) C_β- atoms in covalently linked residues. Also connected are (vi) the beads in the saccharide unit (C_α- and C_β-atoms), and (vii) the covalently linked saccharides within the same carbohydrate cluster. Additional constraint is imposed on the bond angle formed by a triplet of covalently linked residues by adding the repulsive Lennard-Jones potential for the beads separated by two covalent bonds (1–3 interactions)

$$U_{ANG} = \sum_{a=1}^{N_{ang}} \varepsilon_{ang}\left(\sigma_{ang}/r_{ij}\right)^6,$$ where $\varepsilon_{ang} = 1.0$ kcal/mol is the strength of repulsion, and

$\sigma_{ang} = 3.8$ Å is the range of repulsion. In *UANG*, the summation is performed over all N_{ang} bond angles. To account for the non-covalent (non-bonded) interactions that stabilize the

native fold of a biomolecule, we use the harmonic potential $U_{NB}^{ATT} = \sum_{n=1}^{N_{att}} \frac{k_{nat}}{2}\left(r_n - r_n^0\right)^2$

where the summation runs over all N_{att} pairs of beads that are separated by at least 3 covalent bonds and are within the cutoff distance of $r_c = 8$ Å in the initial (or reference) atomic structure; also, r_n^0 is the distance between the two interacting beads and $rn0$ is the corresponding equilibrium distance, taken from the crystal structure ($k_{nat} = 2.0$ kcal/mol Å). The rationale for using the harmonic potential in this case is to constrain the amino acids forming a binary native contact in order to preserve the crystal structure. When sampling the conformational space of fibrin protofibril, we use the full Lennard-Jones potential

$$U_{NB}^{ATT} = \sum_{n=1}^{N_{att}} \varepsilon_n\left[\left(r_n^0/r_n\right)^{12} - 2\left(r_n^0/r_n\right)^6\right]$$ (Zhmurov et al., 2010a). Here ε_n is the strength of the

non-covalent bond, which is usually between 0.6 and 1.3 kcal/mol, depending on the nature of the contact. Using the Lennard-Jones potential allows for the disruption of the native contacts, which is essential while observing the dynamics of the system at equilibrium. The non-native (non-bonded) interactions are treated as repulsive using the Lennard-Jones

potential $U_{NB}^{REP} = \sum_{n=1}^{N_{rep}} \varepsilon_l\left(\sigma_l/r_n\right)^6,$ where the summation runs over all N_{rep} pairs of beads

(C_α- and C_β-atoms) that are neither covalently linked nor form a native contact. We set $\varepsilon_l = 1$ kcal/mol (strength of repulsion) and $\sigma_l = 3.8$ Å (range of repulsion).

Structure Alignment—The Kabsch algorithm (Kabsch, 1976) is a method of finding an orthogonal transformation to overlap one set of atomic coordinates (for one structure) with another set of coordinates (for another structure). We take two structures and then select the atoms that are to be aligned. In our implementation, we use the C_α-atoms in globular parts of the molecule. The two sets of coordinates of N atoms are then organized into two $3 \times N$

matrices X_1 and X_2. Each row of these matrices corresponds to the Cartesian coordinates of atoms from the first molecule (matrix X_1) and second molecule (matrix X_2). Any two rows in the matrix X_1 and matrix X_2 contain two sets of coordinates of atoms (x_1, y_1, z_1) and (x_2, y_2, z_2) to be aligned. Next, we define the unitary rotation matrix $U = \left(A^{\mathrm{T}}A\right)^{1/2}A^{-1}$ where $A = X_1^{\mathrm{T}}X_2$ (superscript T denotes the matrix transpose). To overlap the second molecule with the first, we apply the transformation U to the atomic coordinates in the second molecule. Because the Kabsch algorithm minimizes the root-mean-squared deviations (RMSD) for any pair of structures, this method is widely used in the structure alignment of biomolecules. We utilized this approach in the Elongation procedure (see Figure 1B).

Steepest Descent Energy Minimization and Langevin Simulations—To refine the positions of unresolved parts of fibrin molecule added to the crystal structure, we used CHARMM32 force-field for proteins (MacKerell et al., 1998) and CHARMM36 force-field for carbohydrates (Guvench et al., 2011). To introduce the γ-γ crosslinks, we designed a γ-glutamyl-ε-lysyl patch as described in subsection Transglutamination *in silico* using the atom-type analogy. The system was reconstituted using the CHARMM package (Brooks et al., 2009). The energy minimization was performed using the steepest descent algorithm (Brooks et al., 2009) implemented in our in-house package for GPU-based simulations in implicit solvent (Zhmurov et al., 2012). To preserve the crystal structure, all the resolved parts of the molecules were constrained. We employed the Solvent Accessible Surface Area (SASA) model of implicit solvation (Ferrara et al., 2002), which was re-parameterized to suite CHARMM32/36 force-fields. Next, the energy minimization was performed. We used this approach in the Structure-addition procedure (Figure 1D).

QUANTIFICATION AND STATISTICAL ANALYSIS

Data sample sizes for probability distributions displayed in Figures 4 and 5 are provided in respective figure captions. Average values and standard deviations for data in Figure 4 are presented in Table S2.

DATA AND SOFTWARE AVAILABILITY

Atomic models of fibrin protofibrils are fully available in the form of PDB files for atomic coordinates as Supplementary Data and at http://faculty.uml.edu/vbarsegov/research/fibrin.html.

Supplementary Material

Refer to Web version on PubMed Central for supplementary material.

ACKNOWLEDGMENTS

REFERENCES

Adamczyk Z, Cichocki B, Ekiel-Je ewska ML, Słowicka A, Wajnryb E, and Wasilewska M (2012). Fibrinogen conformations and charge in electrolyte solutions derived from DLS and dynamic viscosity measurements. J. Colloid. Interface Sci 385, 244–257. [PubMed: 22883236]

Alekseenko A, Kononova O, Kholodov Y, Marx KA, and Barsegov V (2016). SOP-GPU: influence of solvent-induced hydrodynamic interactions on dynamic structural transitions in protein assemblies. J. Comput. Chem 37, 1537–1551. [PubMed: 27015749]

Blombäck B, Hessel B, Hogg D, and Therkildsen L (1978). A two-step fibrinogen-fibrin transition in blood coagulation. Nature 275, 501–505. [PubMed: 692730]

Brooks BR, Brooks CL, MacKerell AD, Nilsson L, Petrella RJ, Roux B, Won Y, Archontis G, Bartels C, Boresch S, and Caflisch A (2009). CHARMM: the biomolecular simulation program. J. Comput. Chem 30, 1545–1614. [PubMed: 19444816]

Burton RA, Tsurupa G, Hantgan RR, Tjandra N, and Medved L (2007). NMR solution structure, stability, and interaction of the recombinant bovine fibrinogen αC-domain fragment. Biochemistry 46, 8550–8560. [PubMed: 17590019]

Bura E, Zhmurov A, and Barsegov V (2009). Nonparametric density estimation and optimal bandwidth selection for protein unfolding and unbinding data. J. Chem. Phys 130, 015102. [PubMed: 19140635]

Chernysh IN, Nagaswami C, and Weisel JW (2011). Visualization and identification of the structures formed during early stages of fibrin polymerization. Blood 117, 4609–4614. [PubMed: 21248064]

Doi M, and Edwards SF (1986). The Theory of Polymer Dynamics (New York: Oxford University Press).

Everse SJ, Spraggon G, Veerapandian L, Riley M, and Doolittle RF (1998). Crystal structure of fragment double-D from human fibrin with two different bound ligands. Biochemistry 37, 8637–8642. [PubMed: 9628725]

Everse SJ, Spraggon G, Veerapandian L, and Doolittle RF (1999). Conformational changes in fragments D and double-D from human fibrin(ogen) upon binding the peptide ligand Gly-His-Arg-Pro-amide. Biochemistry 38, 2941–2946. [PubMed: 10074346]

Falvo MR, Millard D, O'Brien ET, Superfine R, and Lord ST (2008). Length of tandem repeats in fibrin's αC region correlates with fiber extensibility. J. Thromb. Haemost 6, 1991–1993. [PubMed: 18761721]

Ferrara P, Apostolakis J, and Caflisch A (2002). Evaluation of a fast implicit solvent model for molecular dynamics simulations. Proteins 46, 24–33. [PubMed: 11746700]

Fischer H, Polikarpov I, and Craievich AF (2004). Average protein density is a molecular-weight-dependent function. Protein Sci 13, 2825–2828. [PubMed: 15388866]

Fowler WE, Hantgan RR, Hermans J, and Erickson HP (1981). Structure of the fibrin protofibril. Proc. Natl. Acad. Sci. USA 78, 4872–4876. [PubMed: 6946434]

Guvench O, Mallajosyula SS, Raman EP, Hatcher E, Vanommeslaeghe K, Foster TJ, Jamison FW, and MacKerell AD Jr. (2011). CHARMM additive all-atom force field for carbohydrate derivatives and its utility in polysaccharide and carbohydrate-protein modeling. J. Chem. Theory Comput 7, 3162–3180. [PubMed: 22125473]

Huang L, Hsiao JPL, Powierza C, Taylor R, and Lord ST (2014). Does topology drive fiber polymerization? Biochemistry 53, 7824–7834. [PubMed: 25419972]

Humphrey W, Dalke A, and Schulten K (1996). VMD: visual molecular dynamics. J. Mol. Graph 14, 33–38. [PubMed: 8744570]

Hunziker EB, Straub PW, and Haeberli A (1988). Molecular morphology of fibrin monomers and early oligomers during fibrin polymerization. J. Ultrastruct. Mol. Struct. Res 98, 60–70. [PubMed: 3351355]

Hyeon C, Dima RI, and Thirumalai D (2006). Pathways and kinetic barriers in mechanical unfolding and refolding of RNA and proteins. Structure 14, 1633–1645. [PubMed: 17098189]

Janmey PA, Winer JP, and Weisel JW (2009). Fibrin gels and their clinical and bioengineering applications. J. R. Soc. Interface 6, 1–10. [PubMed: 18801715]

Kabsch W (1976). A solution for the best rotation to relate two sets of vectors. Acta Crystallogr 32, 922–923.

Klinov DV, Lagutina IV, Prokhorov VV, Neretina T, Khil PP, Lebedev YB, Cherny DI, Demin VV, and Sverdlov ED (1998). High resolution mapping DNAs by R-loop atomic force microscopy. Nucleic Acids Res 26, 4603–4610. [PubMed: 9753727]

Köhler S, Friederike S, and Giovanni S (2015). The internal dynamics of fibrinogen and its implications for coagulation and adsorption. PLoS Comput. Biol 11, e1004346. [PubMed: 26366880]

Kollman JM, Pandi L, Sawaya MR, Riley M, and Doolittle RF (2009). Crystal structure of human fibrinogen. Biochemistry 48, 3877–3886. [PubMed: 19296670]

Kostelansky MS, Betts L, Gorkun OV, and Lord ST (2002). 2.8Å crystal structures of recombinant fibrinogen fragment D with and without two peptide ligands: GHRP binding to the 'b' site disrupts its nearby calcium-binding site. Biochemistry 41, 12124–12132. [PubMed: 12356313]

Litvinov RI, Gorkun OV, Owen SF, Shuman H, and Weisel JW (2005). Polymerization of fibrin: specificity, strength, and stability of knob-hole interactions studied at the single-molecule level. Blood 106, 2944–2951. [PubMed: 15998829]

Litvinov RI, Yakovlev S, Tsurupa G, Gorkun OV, Medved L, and Weisel JW (2007). Direct evidence for specific interactions of the fibrinogen αC-domains with the central E region and with each other. Biochemistry 46, 9133–9142. [PubMed: 17630702]

Litvinov RI, and Weisel JW (2016). What is the biological and clinical relevance of fibrin? Semin. Thromb. Hemost 42, 333–343. [PubMed: 27056152]

Litvinov RI, and Weisel JW (2017). Fibrin mechanical properties and their structural origins. Matrix Biol 60, 110–123. [PubMed: 27553509]

Liu W, Carlisle CR, Sparks EA, and Guthold M (2010). The mechanical properties of single fibrin fibers. J. Thromb. Haemost 8, 1030–1036. [PubMed: 20088938]

MacKerell AD Jr., Bashford D, Bellott M, Dunbrack RL, Evanseck JD, Field MJ, Fischer S, Gao J, Guo H, and Ha S (1998). All-atom empirical potential for molecular modeling and dynamics studies of proteins. J. Phys. Chem. B 102, 3586–3616. [PubMed: 24889800]

Medved L, Ugarova T, Veklich Y, Lukinova N, and Weisel JW (1990). Electron microscope investigation of the early stages of fibrin assembly. Twisted protofibrils and fibers. J. Mol. Biol 216, 503–509. [PubMed: 2258925]

Medved L, Tsurupa G, and Yakovlev S (2001). Conformational changes upon conversion of fibrinogen into fibrin. Ann. N.Y. Acad. Sci 936, 185–204. [PubMed: 11460474]

Moskowitz KA, and Budzynski AZ (1994). The (DD)E complex is maintained by a composite fibrin polymerization site. Biochemistry 33, 12937–12944. [PubMed: 7524657]

Ortega A, Amorós D, and de La Torre JG (2011). Prediction of hydrodynamic and other solution properties of rigid proteins from atomic-and residue-level models. Biophys. J 101, 892–898. [PubMed: 21843480]

Pechik I, Yakovlev S, Mosesson MW, Gilliland GL, and Medved L (2006). Structural basis for sequential cleavage of fibrinopeptides upon fibrin assembly. Biochemistry 45, 3588–3597. [PubMed: 16533041]

Piechocka IK, Jansen KA, Broedersz CP, Kurniawan NA, MacKintosh FC, and Koenderink GH (2016). Multi-scale strain-stiffening of semiflexible bundle networks. Soft Matter 12, 2145–2156. [PubMed: 26761718]

Protopopova AD, Barinov NA, Zavyalova EG, Kopylov AM, Sergienko VI, and Klinov DV (2015). Visualization of fibrinogen αC regions and their arrangement during fibrin network formation by high-resolution AFM. J. Thromb. Haemost 13, 570–579. [PubMed: 25393591]

Protopopova AD, Litvinov R, Galanakis DK, Nagaswami C, Barinov NA, Mukhitov AR, Klinov DV, and Weisel JW (2017). Morphometric characterization of fibrinogen's αC regions and their role in fibrin self-assembly and molecular organization. Nanoscale 9, 13707–13716. [PubMed: 28884176]

Radosevich M, Goubran HA, and Burnouf T (1997). Fibrin sealant: scientific rationale, production methods, properties, and current clinical use. Vox Sang 72, 133–143. [PubMed: 9145483]

Rai N, Nöllmann M, Spotorno B, Tassara G, Byron O, and Rocco M (2005). SOMO (SOlution MOdeler): differences between X-ray-and NMR-derived bead models suggest a role for side chain flexibility in protein hydrodynamics. Structure 13, 723–734. [PubMed: 15893663]

Raynal B, Cardinali B, Grimbergen J, Profumo A, Lord ST, England P, and Rocco M (2013). Hydrodynamic characterization of recombinant human fibrinogen species. Thromb. Res 132, e48–e53. [PubMed: 23642654]

Rocco M, Molteni M, Ponassi M, Giachi G, Frediani M, Koutsioubas A, Profumo A, Trevarin D, Cardinali B, Vachette P, and Ferri F (2014). A comprehensive mechanism of fibrin network formation involving early branching and delayed single-to double-strand transition from coupled time-resolved X-ray/light-scattering detection. J. Am. Chem. Soc 136, 5376–5384. [PubMed: 24654923]

Rosenfeld MA, Leonova VB, Shchegolikhin AN, Bychkova AV, Kostanova EA, and Biryukova MI (2015). Covalent structure of single-stranded fibrin oligomers cross-linked by FXIIIa. Biochem. Biophys. Res. Commun 461, 408–412. [PubMed: 25896761]

Rubinstein M, and Colby RH (2003). Polymer Physics (Oxford U.K: Oxford University Press).

Storm C, Pastore JJ, MacKintosh FC, Lubensky TC, and Janmey PA (2005). Nonlinear elasticity in biological gels. Nature 435, 191–194. [PubMed: 15889088]

Tsurupa G, Hantgan RR, Burton RA, Pechik I, Tjandra N, and Medved L (2009). Structure, stability, and interaction of the fibrin (ogen) αC-domains. Biochemistry 48, 12191–12201. [PubMed: 19928926]

Tsurupa G, Mahid A, Veklich Y, Weisel JW, and Medved L (2011). Structure, stability, and interaction of fibrin αC-domain polymers. Biochemistry 50, 8028–8037. [PubMed: 21806028]

Tsurupa G, Pechik I, Litvinov RI, Hantgan RR, Tjandra N, Weisel JW, and Medved L (2012). On the mechanism of αC polymer formation in fibrin. Biochemistry 51, 2526–2538. [PubMed: 22397628]

Wassenaar TA, Pluhackova K, Böokmann RA, Marrink SJ, and Tieleman DP (2014). Going backward: a flexible geometric approach to reverse transformation from coarse grained to atomistic models. J. Chem. Theory Comput 10, 676–690. [PubMed: 26580045]

Webb B, and Šali A (2017). Protein structure modeling with MODELLER. In Functional Genomics (New York: Humana Press), pp. 39–54.

Weisel JW (1986). Fibrin assembly. Lateral aggregation and the role of the two pairs of fibrinopeptides. Biophys. J 50, 1079–1093. [PubMed: 3801570]

Weisel JW, Nagaswami C, and Makowski L (1987). Twisting of fibrin fibers limits their radial growth. Proc. Natl. Acad. Sci. USA 84, 8991–8995. [PubMed: 3480524]

Weisel JW, and Litvinov RI (2013). Mechanisms of fibrin polymerization and clinical implications. Blood 121, 1712–1719. [PubMed: 23305734]

Weisel JW, and Litvinov RI (2017). Fibrin formation, structure and properties. In Subcellular Biochemistry, *Vol.* 82, Parry DAD and Squire J, eds. (Springer International Publishing), pp. 405–456. [PubMed: 28101869]

Yang Z, Mochalkin I, and Doolittle RF (2000). A model of fibrin formation based on crystal structures of fibrinogen and fibrin fragments complexed with synthetic peptides. Proc. Natl. Acad. Sci. USA 97, 14156–14161. [PubMed: 11121023]

Yang Z, Spraggon G, Pandi L, Everse SJ, Riley M, and Doolittle RF (2002). Crystal structure of fragment D from lamprey fibrinogen complexed with the peptide Gly-His-Arg-Pro-amide. Biochemistry 41, 10218–10224. [PubMed: 12162736]

Zhmurov A, Dima RI, Kholodov Y, and Barsegov V (2010a). SOP-GPU: Accelerating biomolecular simulations in the centisecond timescale on graphics processors. Proteins 78, 2984–2999. [PubMed: 20715052]

Zhmurov A, Rybnikov K, Kholodov Y, and Barsegov V (2010b). Generation of random numbers on graphics processors: forced indentation in silico of the bacteriophage HK97. J. Phys. Chem. B 115, 5278–5288. [PubMed: 21194190]

Zhmurov A, Brown AEX, Litvinov RI, Dima RI, Weisel JW, and Barsegov V (2011). Mechanism of fibrin (ogen) forced unfolding. Structure 19, 1615–1624. [PubMed: 22078561]

Zhmurov A, Kononova O, Litvinov RI, Dima RI, Barsegov V, and Weisel JW (2012). Mechanical transition from α-helical coiled coils to β-sheets in fibrin(ogen). J. Am. Chem. Soc 134, 20396–20402. [PubMed: 22953986]

Zhmurov A, Protopopova AD, Litvinov RI, Zhukov P, Mukhitov AR, Weisel JW, and Barsegov V (2016). Structural basis of interfacial flexibility in fibrin oligomers. Structure 24, 1907–1917. [PubMed: 27692965]

Zuev YF, Litvinov RI, Sitnitsky AE, Idiyatullin BZ, Bakirova DR, Galanakis D, Zhmurov A, Barsegov V, and Weisel JW (2017). Conformational flexibility and self-association of fibrinogen in concentrated solutions. J. Phys. Chem. B 121, 7833–7843. [PubMed: 28742964]

Highlights

- Atomic structures of fibrin oligomers and protofibrils are reconstructed *in silico*

- Structural models show good agreement with high-resolution AFM images

- Fibrin protofibrils are double-stranded twisted oligomers that can bend and kink

- Hydrodynamic parameters of fibrin oligomers and protofibrils are calculated
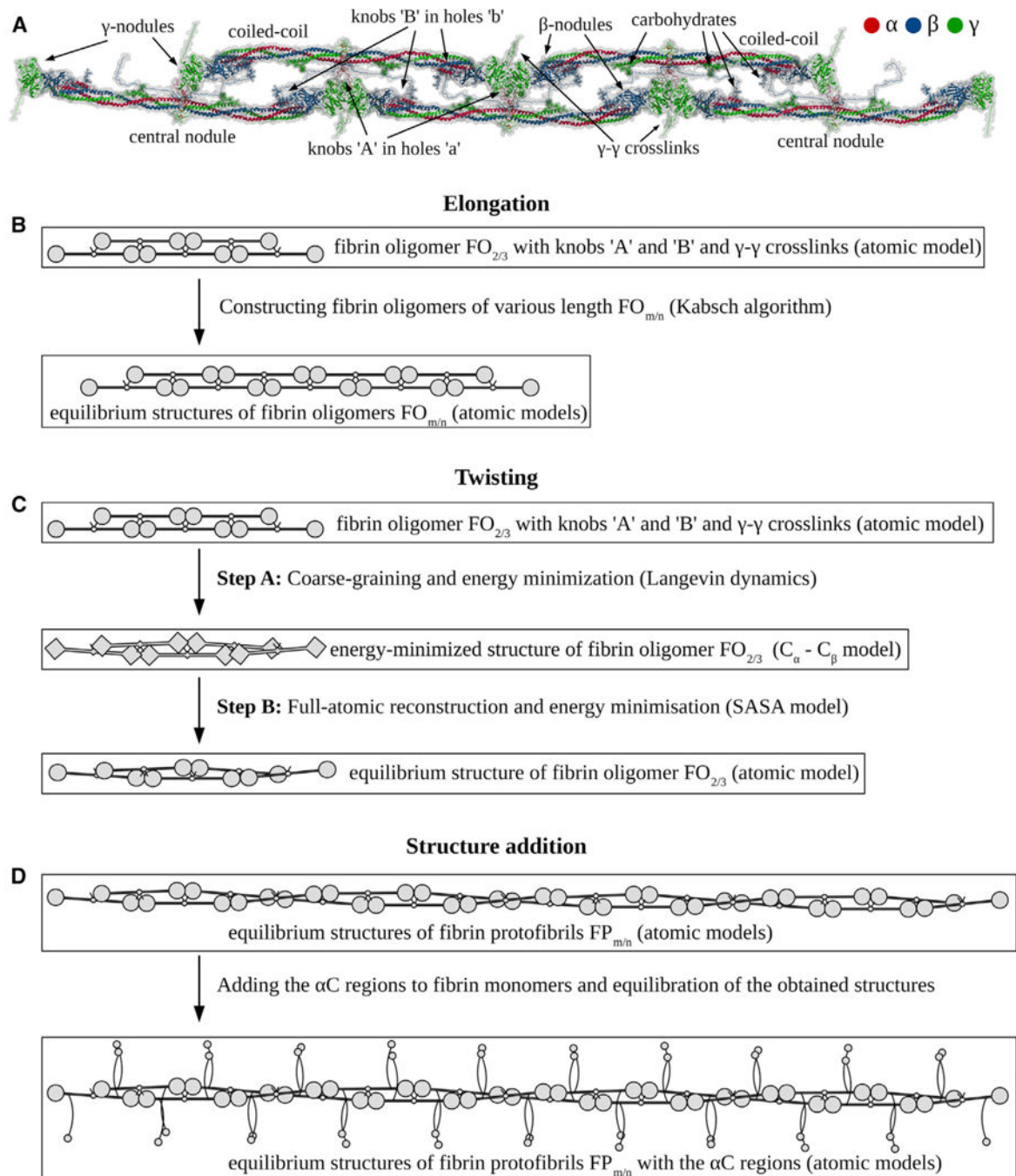
Figure 1.
From Fibrin Oligomer to Fibrin Protofibril Based on Computational Crystallomics (A) Structure of short fibrin oligomer FO$_{2/3}$ used as an elementary building block, which contains five fibrin monomers (Zhmurov et al., 2016). (B) Schematic of elongation procedure used to reconstruct longer oligomers FO$_{m/n}$ starting from short oligomers FO$_{2/3}$ as described in the text (Results; see also STAR Methods and Figure S1). (C) Workflow involved in introducing the twist into the structure of fibrin oligomers and protofibril as described in the text (Results; see also STAR Methods). (D) Final stage of protofibril
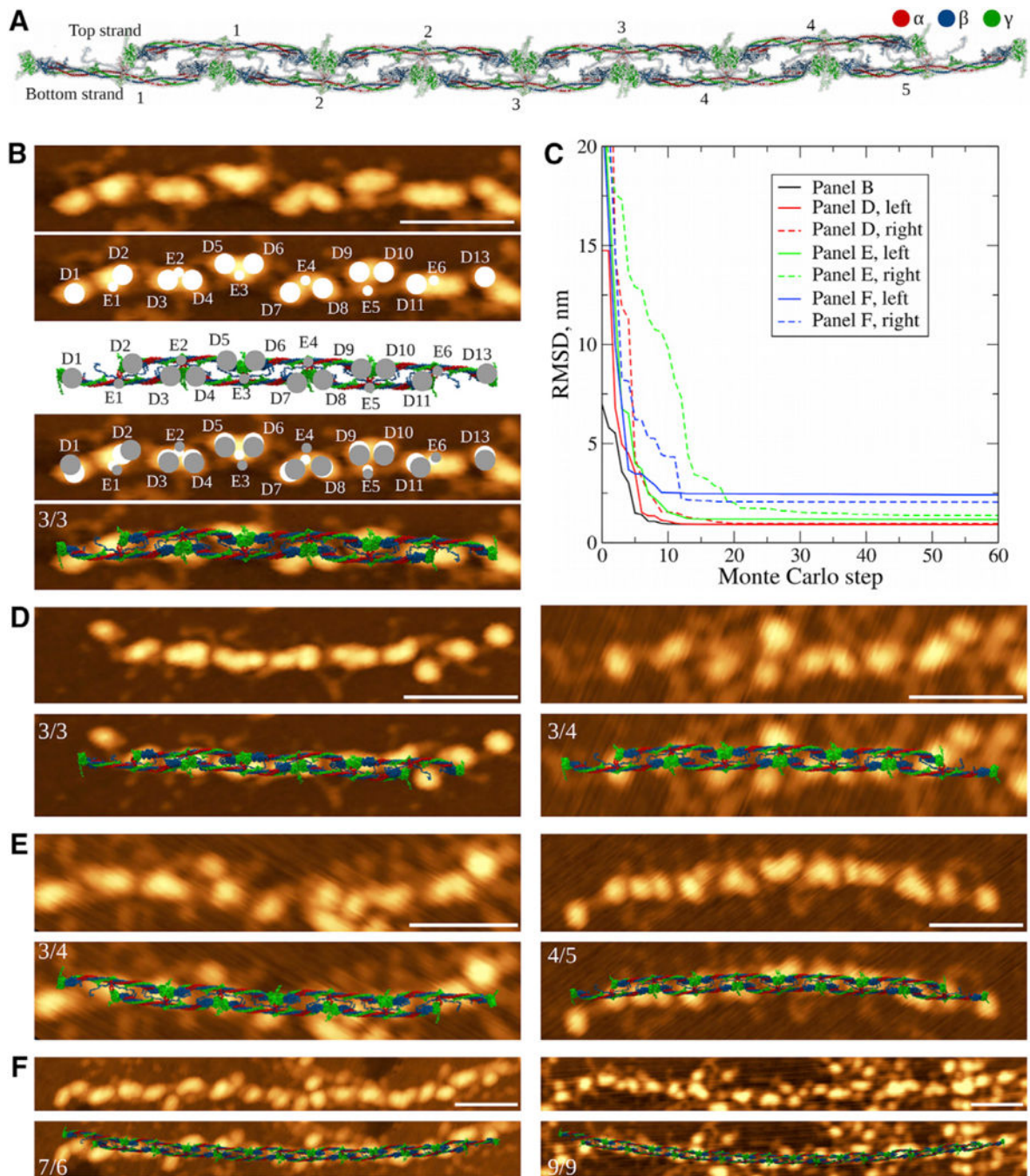
reconstruction, in which all steric clashes are removed and the αC chains are incorporated (Results; see also STAR Methods).

Figure 2.

Comparison of Fibrin Oligomer Structures Obtained *In Silico* and *In Vitro* (A) Structure of double-stranded fibrin oligomer $FO_{4/5}$, obtaining using an elongation procedure (Figure 1B) applied to a short fibrin oligomer $FO_{2/3}$ with the straight conformation of D:D self-association interface (STAR Methods). (B) Monte Carlo method used to overlap the atomic structural models with AFM images. We identify the positions of geometric centers of the globular D and E regions in an AFM image (white circles) and centers of mass of these regions in the atomic structure of equal length (gray circles). Monte Carlo simulations are

used to perform rigid-body transformation that minimizes the RMSD between positions of the globular regions (fourth image). Similar transformation is then applied to the atomic structure (last image). (C) Dynamics of RMSD values between the globular regions identified in AFM images and atomic structural models from Monte Carlo simulations. Shown are curves for the structure overlaps presented in (B), (D), (E), and (F). (D–F) Structures of the fibrin oligomers of various length overlaid with the AFM images. Short oligomers (D) show very good agreement with the experimental AFM data. With increasing length of fibrin oligomers reconstructed using the straight conformation of the D:D interface, the agreement becomes worse (E), and structures of longer oligomers ($FO_{5/6}$ or longer) come short at explaining the overall shape and structural features observed experimentally (F). On each AFM image the numerals indicate the number of fibrin monomers in the upper/lower strands. Scale bars, 50 nm.
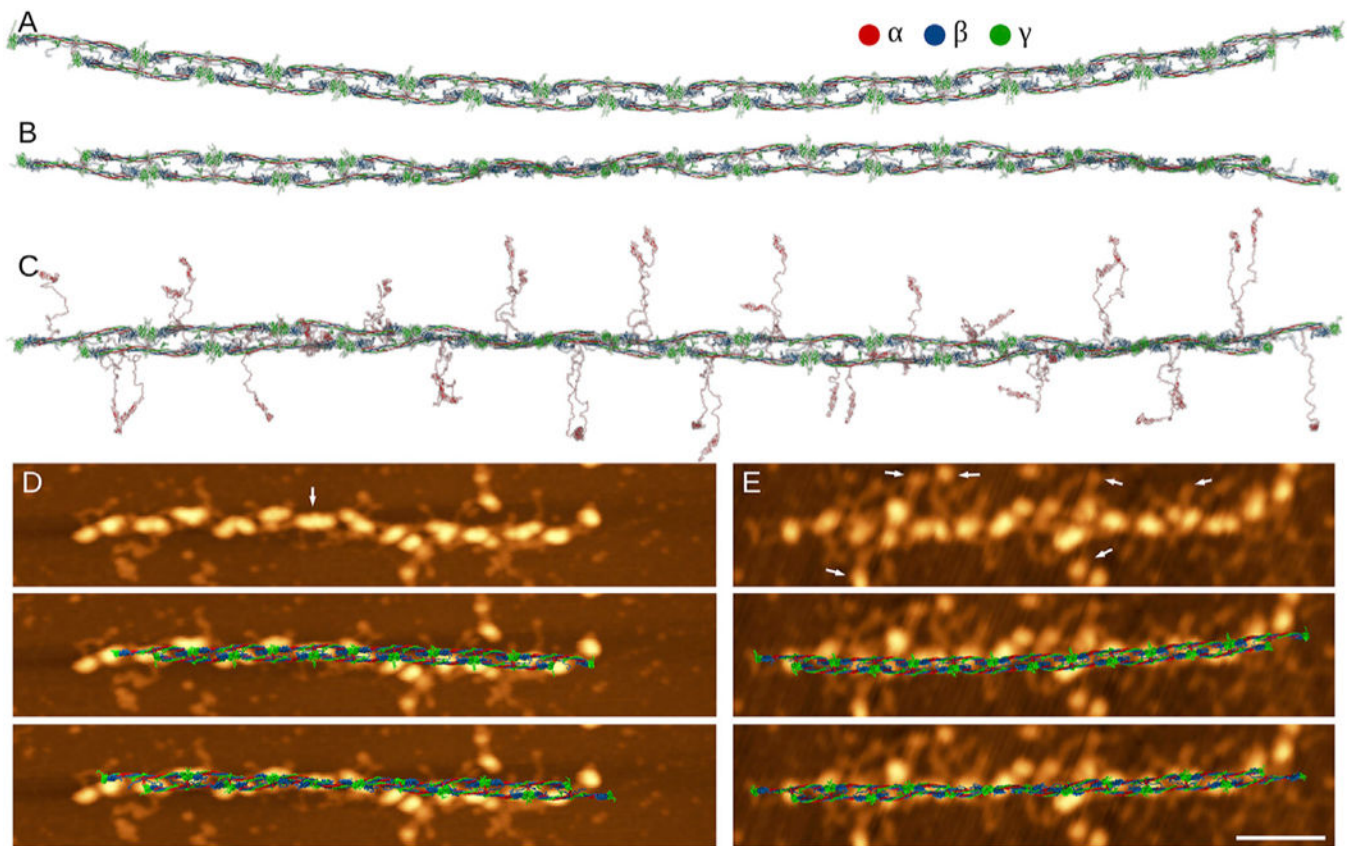
Figure 3.

Comparison of Structures of Fibrin Protofibril FP$_{9/10}$ Obtained *In Silico* and *In Vitro* (A)
Atomic model of FP$_{9/10}$ with a straight conformation of D:D interface (PDB: 1N86)
obtained using the elongation procedure (Figure 1B). (B) Atomic model of FP$_{9/10}$ with a
twisted conformation of D:D interface (PDB: 1FZG) obtained using the twisting procedure
followed by the elongation step (Figures 1C and 1B). This structure was equilibrated using
Langevin simulations of the SOP model of FP$_{9/10}$, then back-mapped and energy-minimized
in the full-atomic representation (see also Figure S2). (C) Energy-minimized structure of
FP$_{9/10}$ as in (B) but with the αC regions (structure-addition step in Figure 1C). See also Data
S1 and S2. (D and E) Atomic models of fibrin protofibril backbones (shown without the αC
regions for clarity) of different size and shape (straight and bent conformations)
reconstructed *in silico* are overlaid with the high-resolution AFM images of fibrin
protofibrils. The white arrow in (D) indicates the position along the oligomer where the
trinodular structure of D-E-D construct is not visible, which suggests twisting of the
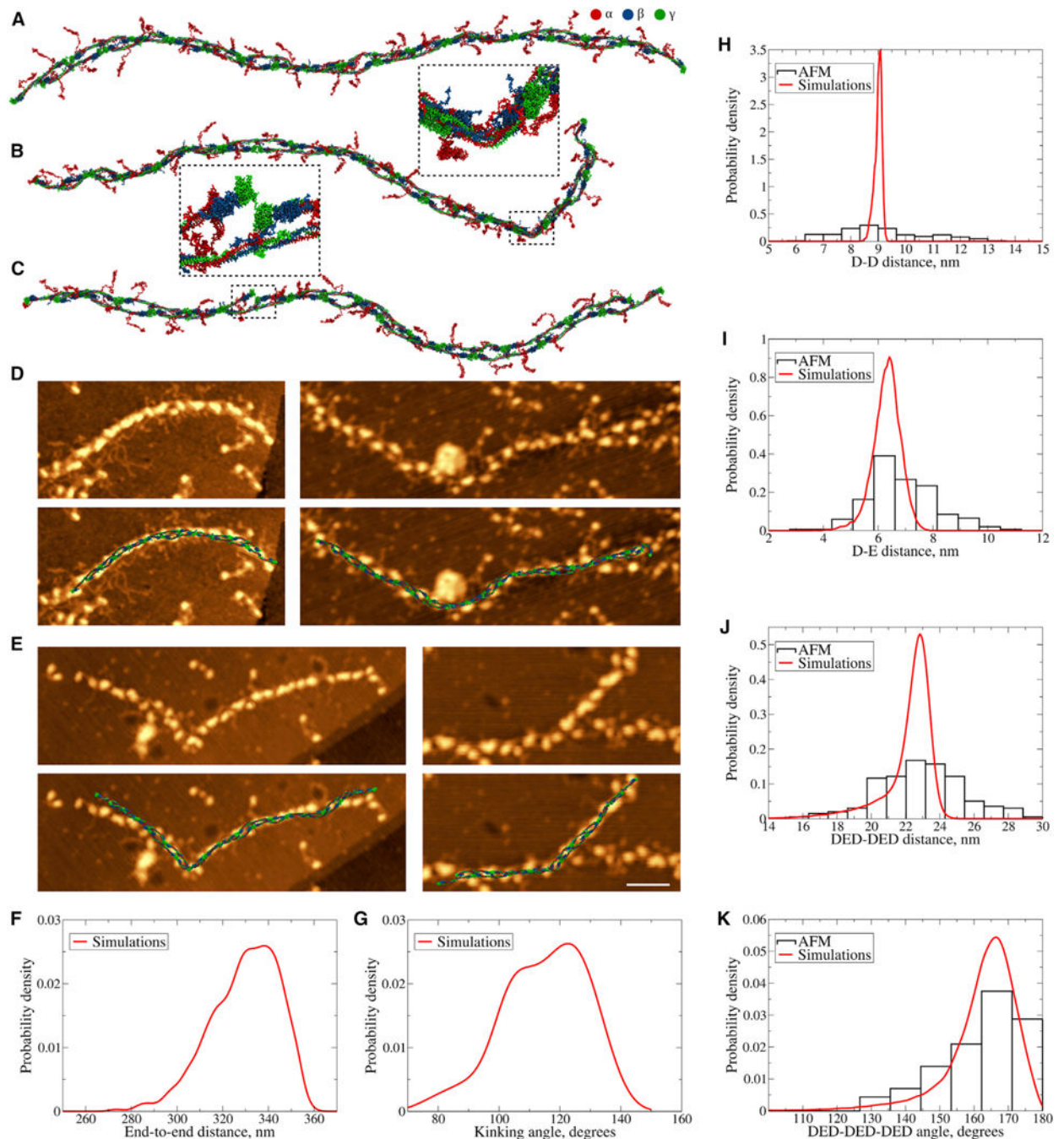structure. The arrows in (E) show the position of αC domains. Scale bar, 50 nm.

Figure 4.
Conformational Dynamics of Fibrin Protofibrils (A) Structure of $FP_{9/10}$ in a coarse-grained representation used to study the equilibrium dynamics of fibril protofibrils. (B) Structure showing a kink formed in the unstructured regions of α-helical coiled coils in both strands (magnified in the inset). (C) Structure with dissociated A:a knob-hole bond. The A:a knob-hole bond dissociation is followed by the disruption of D:D self-association interface (magnified in the inset). (D and E) Representative high-resolution AFM images of bent fibrin protofibrils (D) and protofibrils with kinks (E) overlaid with the corresponding

structures obtained *in silico*. Scale bar, 50 nm. (F and G) Probability distributions of the end-to-end distances (F, sample size = 1,000) and kinking angles (G, sample size = 51) from equilibrium simulations of fibrin protofibrils obtained using kernel density estimation with the Gaussian kernel (Bura et al., 2009). (H–K) Probability distributions of the distances between two adjacent D regions (H, sample size = 153 for AFM and 100,000 for simulations), between D and E regions in the DED complex (I, sample sizes = 200 and 200,000), between two consecutive DED complexes (J, sample sizes = 173 and 92,000), and probability distributions of angles made by three consecutive DED complexes (K, sample sizes = 129 and 67,000) from AFM experiments (histograms) and equilibrium MD simulations (curves). Theoretical distributions were obtained using kernel density estimation with the Gaussian kernel (Bura et al., 2009). See also Table S2.
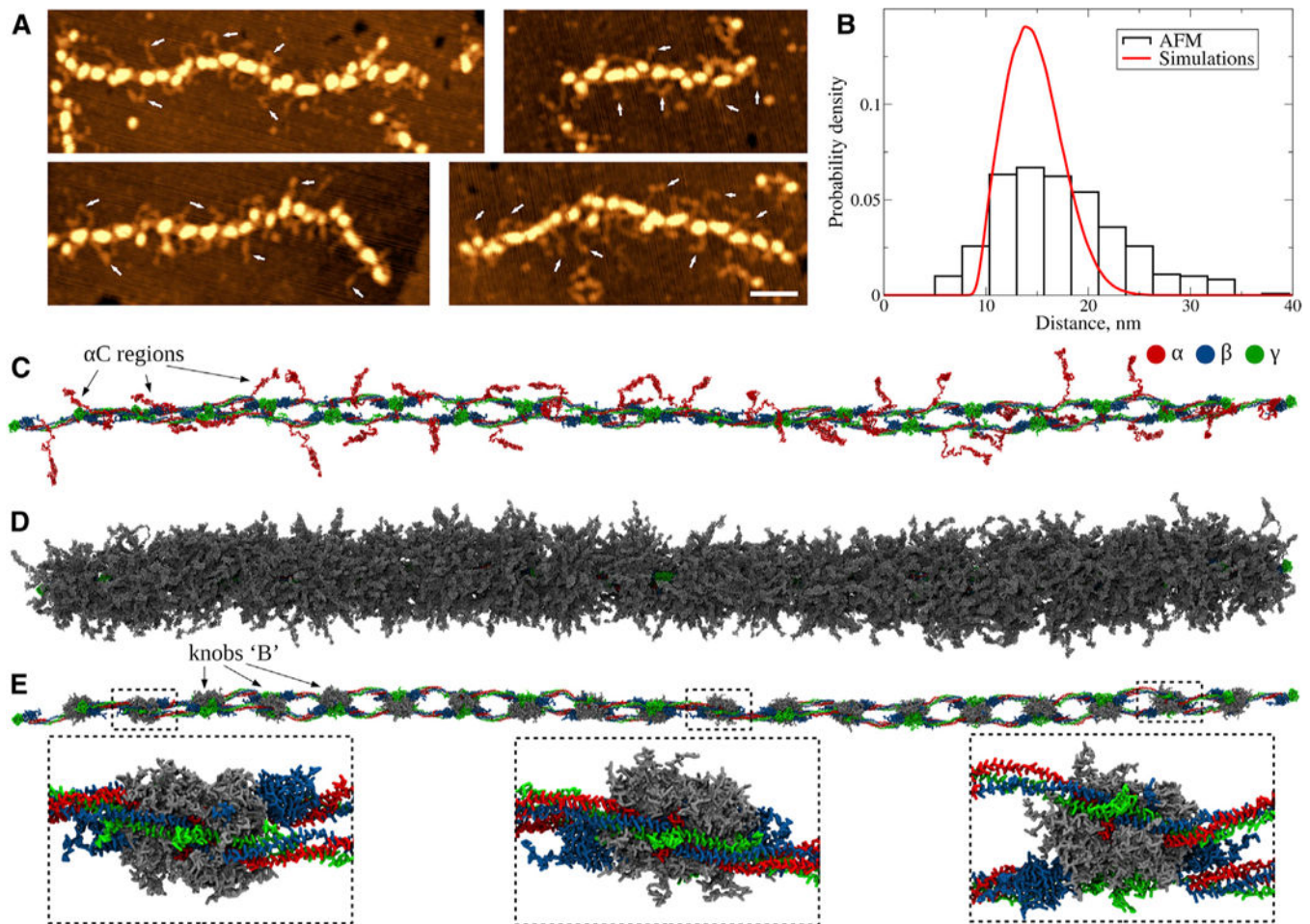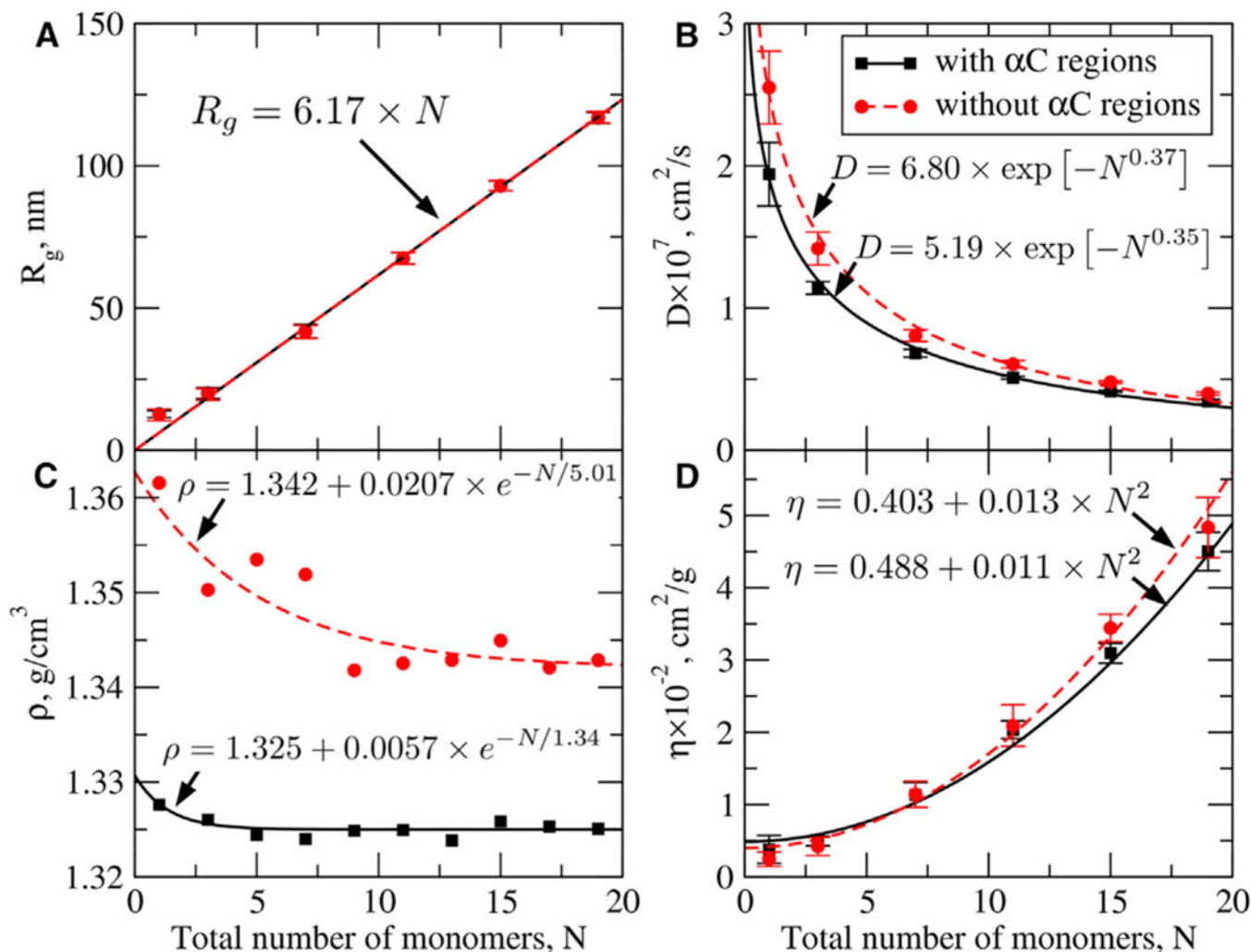
Figure 5.
Dynamics of αC Regions and Knobs ''B'' (A) AFM images of fibrin protofibrils: the top image shows multiple αC regions protruding from the protofibril backbone (indicated by the arrows). Scale bar, 50 nm. (B) Experimental and theoretical probability distributions of the distances between the ends of αC regions and the protofibril backbone. Experimental distribution from AFM images is colored red (sample size = 410); theoretical distribution obtained using kernel density estimation with the Gaussian kernel (Bura et al., 2009) from five simulation runs is colored black (sample size = 50,000). (C) Structure of fibrin protofibrils from Langevin simulations of $FP_{9/10}$ in a coarse-grained representation with the protofibril backbone constrained. (D) Same structure as in (C) superposed with an ensemble of conformations of αC regions (shown in gray). (E) Same structure as in (D) superposed with an ensemble of conformations of knobs ''B'' (magnified in the insets).

A — $R_g = 6.17 \times N$

B — $D = 6.80 \times \exp\left[-N^{0.37}\right]$; $D = 5.19 \times \exp\left[-N^{0.35}\right]$

— with αC regions
— without αC regions

C — $\rho = 1.342 + 0.0207 \times e^{-N/5.01}$; $\rho = 1.325 + 0.0057 \times e^{-N/1.34}$

D — $\eta = 0.403 + 0.013 \times N^2$; $\eta = 0.488 + 0.011 \times N^2$

Figure 6.

Molecular (Hydro)Dynamic Parameters for Double-Stranded Fibrin Polymers (with and without αC Regions; Based on Data in Table 1) (A–D) Shown are the profiles of the radius of gyration (R_g; A), translational diffusion coefficient (D; B), protein density (ρ; C), and intrinsic viscosity (η; D) as a function of size $N = n + m$ (n/m are the numbers of monomers in the first/second strands). Analytical expressions approximating these quantities as functions of N (formulas) and results of numerical fitting (curves) are displayed on the graphs. We used a linear function for R_g, stretched exponential functions for D, exponential function for ρ, and quadratic function for η. Calculated values of hydrodynamic parameters (data points) are accumulated in Table 1. Data for the full-length (truncated) fibrin molecules are shown as black squares (red circles) with the solid (dashed) black (red) line for analytical fit. Error bars in (A), (B), and (D) are standard deviations.

REAGENT or RESOURCE	SOURCE	IDENTIFIER
Biological Samples		
Human fibrinogen	Hyphen BioMed, France	Cat#PP001
Thrombin	Sigma Aldrich, USA	T4393; CAS: 9002–04-4
Deposited Data		
Structure of human fibrinogen monomer	Kollman et al., 2009	PDB: 3GHG
Structure of D-dimer from human fibrinogen in bent conformation	Everse et al., 1999	PDB: 1FZG
Structure of D-dimer from human fibrinogen in straight conformation	Yang et al., 2002	PDB: 1N86
Structure of bovine fibrinogen aC-domain	Burton et al., 2007	PDB: 2JOR
Software and Algorithms		
VMD	Humphrey et al., 1996	http://www.ks.uiuc.edu/Research/vmd/
CHARMM	Brooks et al., 2009	https://www.charmm.org/
MODELLER	Webb and Sali, 2017	https://salilab.org/modeller/
HYDROPRO	Ortega et al., 2011	http://leonardo.inf.um.es/macromol/programs/hydropro/hydropro.htm
US-SOMO	Rai et al., 2005	http://www.somo.uthscsa.edu/
SOP-GPU	Zhmurov et al., 2010a	http://sop-gpu.readthedocs.io
MDis	Zhmurov et al., 2012	https://github.com/zhmurov/MDis
FemtoScan Online software	Advanced Technologies Center	http://www.femtoscanonline.com
XMGrace	Grace Development Team	http://plasma-gate.weizmann.ac.il/Grace/
Other		
Atomic models of fibrin protofibrils	This paper	http://faculty.uml.edu/vbarsegov/research/fibrin.html
Atomic force microscope	Asylum Research - Oxford Instruments, USA	MFP-3D Classic AFM
Cantilevers for atomic force microscopy	Klinov et al., 1998	N/A

Table 1.

Molecular Parameters of Fibrin Monomer, Oligomers $FO_{n/m}$, and Protofibril $FP_{9/10}$ Calculated Based on the Atomic Models Reconstructed *In Silico* with and without the αC Regions: Molar Mass (M), Radius of Gyration (R_g), Diffusion Coefficient (D), Density (ρ), and Intrinsic Viscosity (η)

Constructs	M (G/mol)	R_g (nm)	D (cm2/s)		ρ (g/cm3)	η (cm3/g)
Fibrin(ogen) monomers						
Truncated des-αC fibrin monomer	246,395	12.5 ± 2.0	$(2.5 \pm 0.3) \times 10^{-7}$		1.361	24 ± 9
Full-length fibrin monomer	332,418	12.7 ± 1.3	$(1.9 \pm 0.2) \times 10^{-7}$		1.328	38 ± 19
Double-stranded fibrin oligomers/protofibril without the αC regions						
$FO_{1/2}$	739,185	12.5 ± 2.0	$(1.4 \pm 0.1) \times 10^{-7}$		1.350	42 ± 12
$FO_{3/4}$	1,724,765	19.6 ± 2.1	$(8.1 \pm 0.4) \times 10^{-8}$		1.352	114 ± 18
$FO_{5/6}$	2,710,345	41.6 ± 2.2	$(6.0 \pm 0.3) \times 10^{-8}$		1.346	209 ± 29
$FO_{7/8}$	3,695,925	67.5 ± 2.1	$(4.79 \pm 0.08) \times 10^{-8}$		1.344	344 ± 19
$FP_{9/10}$	4,681,505	117.1 ± 2.0	$(4.0 \pm 0.1) \times 10^{-8}$		1.342	483 ± 42
Double-stranded fibrin oligomers/protofibril with the αC regions						
$FO_{1/2}$	997,254	20.1 ± 1.9	$(1.14 \pm 0.04) \times 10^{-7}$		1.326	50 ± 7
$FO_{3/4}$	2,326,926	41.8 ± 2.4	$(6.8 \pm 0.2) \times 10^{-8}$		1.325	113 ± 17
$FO_{5/6}$	3,656,598	67.5 ± 2.0	$(5.1 \pm 0.1) \times 10^{-8}$		1.325	204 ± 12
$FO_{7/8}$	4,986,270	93.0 ± 1.7	$(4.15 \pm 0.07) \times 10^{-8}$		1.324	309 ± 14
$FP_{9/10}$	6,315,942	116.8 ± 1.9	$(3.4 \pm 0.2) \times 10+$		1.324	450 ± 27

The values of R_g, D, ρ, and η are for 20°C.